# J|A|C|S

JOURNAL OF THE AMERICAN CHEMICAL SOCIETY

Article

pubs.acs.org/JACS

Epitaxial Stabilization between Intermetallic and Carbide Domains in the Structures of $Mn_{16}SiC_4$ and $Mn_{17}Si_2C_4$

Rie T. Fredrickson, Yiming Guo, and Daniel C. Fredrickson*

Department of Chemistry, University of Wisconsin−Madison, 1101 University Avenue, Madison, Wisconsin 57306, United States

S *Supporting Information*

ABSTRACT: The concept of frustration between competing geometrical or bonding motifs is frequently evoked in explaining complex phenomena in the structures and properties of materials. This idea is of particular importance for metallic systems, where frustration forms the basis for the design of metallic glasses, a source of diverse magnetic phenomena, and a rationale for the existence of intermetallics with giant unit cells containing thousands of atoms. Unlike soft materials, however, where conflicts can be synthetically encoded in the molecular structure, staging frustration in the metallic state is challenging due to the ease of macroscopic segregation of incompatible components. In this Article, we illustrate one approach for inducing the intergrowth of incompatible bonding motifs with the synthesis and characterization of two new intermetallic carbides: $Mn_{16}SiC_4$ ($mC42$) and $Mn_{17}Si_2C_4$ ($mP46$). Similar to the phases Mn_5SiC and Mn_8Si_2C in the Mn−Si−C system, these compounds appear as intergrowths of Mn_3C and tetrahedrally close-packed (TCP) regions reminiscent of Mn-rich Mn−Si phases. The nearly complete spatial segregation of Mn−Si (intermetallic) and Mn−C (carbide) interactions in these structures can be understood from the differing geometrical requirements of C and Si. Rather than macroscopically separating into distinct phases, though, the two bonding types are tightly interwoven, with most Mn atoms being on the interfaces. DFT chemical pressure analysis reveals a driving force stabilizing these interfaces: the major local pressures acting between the Mn atoms in the Mn−Si and Mn−C systems are of opposite signs. Joining the intermetallic and carbide domains together then provides substantial relief to these local pressures, an effect we term epitaxial stabilization.
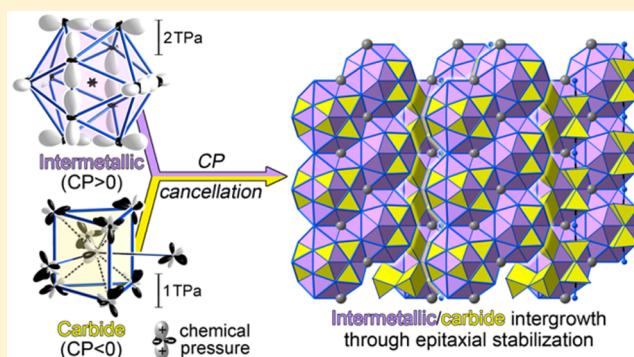
1. INTRODUCTION

A major endeavor in materials chemistry is the cultivation of frustration at the scale of interatomic interactions. Beautiful phase morphologies are continually being revealed in amphiphilic systems where the incompatible domains struggle to minimize their surface area, while being inextricably tied together by covalent linkages.[1] Similarly, metallic liquids and glasses are frequently discussed in terms of structural motifs optimal for local packing (such as tetrahedra) and the frustration encountered in attempting to propagate these units into periodic structures.[2−6] Design principles for metallic glasses then focus on enhancing these difficulties in atomic packing to impede the process of crystallization.[7−9] Similar ideas have been extended to make sense of complex intermetallic crystal structures, including the notion of incompatible packing or bonding modes interpenetrating each other to create giant unit cells.[10−12] Finally, diverse magnetic phenomena arise from magnetic frustration, in which the topologies of spin−spin interactions prevent all spin pairings from being satisfied simultaneously.[13−17] The ability to induce frustration is thus one of the keys to the discovery of new materials and properties.

While in soft materials frustration can be designed in the structure of a molecule, the situation is more challenging for metallic systems. Frustrated interactions in the packing of metals are usually created through the use of multinary systems, where many types of interatomic interactions and atomic size requirements must be reconciled. With this strategy, however, one must always compete against the freedom of the atoms in a metallic system to phase segregate, which often results in a race against the crystallization of separate phases. A broader range of new metallic systems could be accessed if analogues could be developed to the covalent linkages that connect the opposing domains in surfactants or block copolymers.

One possible means for stabilizing such interfaces in metallic systems arose during our examination of the complex quasicrystal approximant structure of $Ca_{10}Cd_{27}Cu_2$.[18] DFT-chemical pressure analysis on related binary phases revealed that the nearby Ca−Cd and Cu−Cd phases exhibit complementary local pressures. In the $MgZn_2$-type $CaCd_2$ phase, the Ca−Cd interactions show negative pressures, indicating that they would be stabilized by contraction of the

structure. Cu_2Cd_5, on the other hand, contains a number of Cu−Cd contacts suffering from positive pressure, which would benefit energetically from the expansion of the structure. The joining of Ca- and Cu-centered Cd polyhedra, as occurs in $Ca_{10}Cd_{27}Cu_2$, offers a means of alleviating these local pressures, as the desired expansion of the Cu-centered polyhedra would correlate with a contraction of the Cd-centered ones. This mechanism for intergrowth formation might be considered a form of *epitaxial stabilization*, the reverse of the destabilizing epitaxial strain usually present at coherent interfaces between materials.[19]

In this Article, we present two new compounds (in a very different system) which support this mechanism of chemical pressure-driven intergrowth: $Mn_{16}SiC_4$ and $Mn_{17}Si_2C_4$. Like other ternary carbide systems, the Mn−Si−C system has a strong potential for exhibiting frustrated interactions (Figure 1). Intermetallic binaries frequently exhibit tetrahedral close-
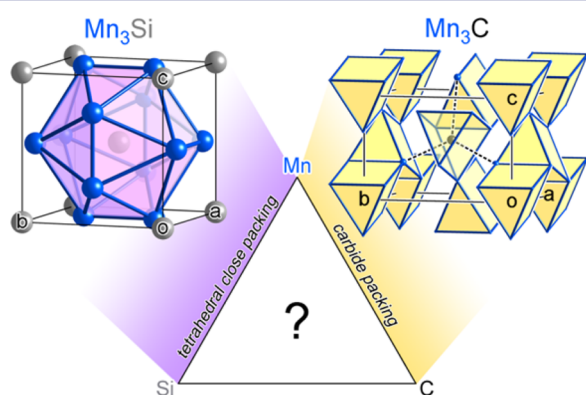

Figure 1. Scheme for inducing frustration in the Mn−Si−C system. Mn-rich Mn−Si phases tend to adopt tetrahedral close-packed (TCP) structures (illustrated here, for simplicity, by a hypothetical Cr_3Si-type Mn_3Si phase). Carbon, however, requires larger coordination environments than those offered by TCP geometries, such as the capped trigonal prisms in Mn_3C.

packed (TCP) geometries, in which all interstitial spaces take the form of distorted tetrahedra.[20] Such geometries are prevalent on the Mn-rich side of the Mn−Si system, as is illustrated with the structures of α-Mn[21] and ν-$Mn_{81.5}Si_{18.5}$.[22] In metal carbides, however, carbon atoms generally prefer larger coordination environments than would be provided by tetrahedral holes, such as octahedra or trigonal prisms, the latter of which are found in the Mn−C binary phase Mn_3C.[23] This system is thus charged with reconciling these competing desires for TCP arrangements and larger spaces to host C atoms,[24] a theme that may help explain the diversity encountered in metal-rich carbides.[25−30]

Macroscopic segregation into separate Mn−Si and Mn−C phases would thus seem to be a likely outcome. However, as we will see, mixing these interactions creates the opportunity for epitaxial stabilization: the Mn-rich phases Mn_3C and Mn_3Si exhibit complementary chemical pressure schemes that could find relief at an interface between them. This driving force explains not only the formation of the new phases $Mn_{16}SiC_4$ and $Mn_{17}Si_2C_4$ but also some general details of their crystal structures. Distinct TCP and carbide domains can be perceived in each of their structures, with the vast majority of the Mn atoms residing at the interfaces between the two domain types. Indeed, together with the previously reported phases

Mn_5SiC[31,32] and Mn_8Si_2C,[33,34] these compounds build up a series of intergrowths between the carbide phase Mn_3C and a TCP Cr_3Si-type Mn_3Si phase (a likely candidate for the as yet unsolved low-temperature polymorph of Mn_3Si[35]). This intergrowth series provides an illustration of the structural diversity which might be accessed through frustration in intermetallic systems, with the epitaxial stabilization mechanism serving as one possible guide.

2. EXPERIMENTAL SECTION

Syntheses. In our synthetic investigations of the Mn−Si−C system, Mn (Alfa Aesar, 99.95%), Si (Strem chemicals, 99.999%), and C (Strem chemicals, 99.998%) were used as starting materials. For the syntheses of $Mn_{16}SiC_4$ (I) and $Mn_{17}Si_2C_4$ (II), the elements were weighed in the stoichiometric molar ratios of Mn/Si/C = 16:1:4(I) or 17:2:4(II) in an Ar filled glovebox. The materials were pressed into pellets and then welded with an arc melting furnace on a copper hearth three times on alternating sides for optimal homogeneity. The arc-melted alloys were placed into fused silica tubes under an Ar atmosphere, which were then evacuated and sealed. The tubes were annealed at 1000 °C in a muffle furnace for 168 h (I) and 1100 °C for 120 h (II) and then cooled to ambient temperature at the fastest rate accessible by the furnace.

Single Crystal X-ray Diffraction Analysis. Single crystal X-ray diffraction data for $Mn_{16}SiC_4$ and $Mn_{17}Si_2C_4$ were collected on an Oxford Diffraction Xcalibur E diffractometer using graphite mono-chromatized Mo Kα radiation (λ = 0.7173 Å) at ambient temperature. The collection and processing of the data set were performed using the CrysAlis Pro v.171.35.15 software supplied by the manufacturer. The structure was solved with the charge flipping algorithm[36,37] using the program SUPERFLIP[38] and refined on F^2 using the program JANA2006.[39] Further details regarding the refinements are given in Table 1 and the Supporting Information.

Table 1. Selected Crystal Data for $Mn_{16}SiC_4$ and $Mn_{17}Si_2C_4$[a]

Chemical formula	$Mn_{16}SiC_4$	$Mn_{17}Si_2C_4$
WDS composition	$Mn_{16}Si_{0.917(10)}C_{4.14(6)}$	$Mn_{17}Si_{1.781(14)}C_{4.16(9)}$
Space group	$C2/m$	$P2_1/m$
Unit cell a [Å]	10.280(3)	6.4114(9)
Unit cell b [Å]	7.7913(19)	7.6648(5)
Unit cell c [Å]	6.3715(16)	10.4946(16)
Unit cell $β$ [deg]	119.12(3)	106.247(13)
Cell volume	445.8(2)	495.13(11)
Z	2	2
Radiation source, λ [Å]	Mo, Kα [0.7107]	Mo, Kα [0.7107]
Number of reflections	2132	4268
Unique refl. [$I > 3σ(I)$, all]	437, 567	950, 1250
R_{int} [$I > 3σ(I)$, all]	4.47, 4.83	4.84, 5.10
Number of parameters	55	55
$R[I > 3σ(I)]$, $R_w[I > 3σ(I)]$	0.0265, 0.0466	0.0329, 0.0505
R(all), R_w(all)	0.0459, 0.0536	0.0338, 0.0383
$S[I > 3σ(I)]$, S(all)	1.12, 1.11	1.19, 1.16
$Δρ_{max}$, $Δρ_{min}(e^-/Å^{-3})$	1.08, −1.04	1.17, −1.24

[a]Additional data are given in Table S1 of the Supporting Information.

Powder X-ray Diffraction Analysis. The phase purities of the samples were checked using powder X-ray diffraction measurements. Each sample was ground to a fine powder and placed on a zero-background plate. Diffraction intensities were measured on a Bruker D8 Advance Powder Diffractometer fitted with an LYNXEYE detector, using Cu Kα radiation (λ = 1.5418 Å) at ambient temperature (exposure time of 1.0 s per 0.015° increment over the 2θ range of 30°−60°). The powder X-ray diffraction patterns collected for the phases are given in the Supporting Information.

Electron Probe Micro Analysis. For the determination of the elemental composition of $Mn_{16}SiC_4$ and $Mn_{17}Si_2C_4$, electron probe micro analysis (EPMA) was performed with a Cameca SX51 electron microprobe (15 kV and 20 nA) on samples prepared as described in the Supporting Information. Mn metal (freshly polished) and SiC were used as standards, leading to the sums of the percentages being close to 100%. Data analysis was carried out with the Probe for EPMA software.[40] For the $Mn_{16}SiC_4$ sample, the measured composition of the major phase was $Mn_{16}Si_{0.917(10)}C_{4.14(6)}$ (average of 20 measurement points). For the $Mn_{17}Si_2C_4$ sample, the major phase had the composition $Mn_{17}Si_{1.781(14)}C_{4.16(9)}$ (average of 20 measurement points), with the remaining phases corresponding to Mn−C binary phases.

Magnetic Property Measurements. For magnetic properties measurements, new samples were synthesized containing $Mn_{16}SiC_4$, $Mn_{17}Si_2C_4$, or Mn_5SiC as major phases (as confirmed with powder X-ray diffraction). These samples were then ground to a fine powder and placed in a Teflon cup attached to a carbon fiber rod. Magnetic susceptibility and hysteresis measurements were performed on the samples with a Quantum Design Physical Property Measurement System (PPMS-9T) equipped with a Vibrating Sample Magnetometer (VSM).

Electronic Structure Calculations. DFT-Chemical Pressure analyses (DFT-CP)[41−43] were carried out on the LDA-DFT electronic structures of various phases in the Mn−Si−C system (Mn_3Si, Mn_3C, $Mn_{16}SiC_4$, $Mn_{17}Si_2C_4$, and Mn_5SiC). These analyses began with the full geometrical optimization of the crystal structures with the Vienna Ab initio Simulation Package (VASP)[44,45] in the high precision mode, using the ultrasoft LDA pseudopotentials provided with the package.[46] Single-point calculations were carried out on the optimized structures with the ABINIT program[47,48] (with LDA-DFT[49] and norm-conserving pseudopotentials[50]) at a series of volumes (equilibrium volume, as well as slightly expanded and contracted cells) to obtain the kinetic energy and electron densities, and the various components of the local potential needed for the construction of CP maps. CP maps were generated from the ABINIT output with *CPmap* and integrated with *CPint*,[51] using the core undistorting procedure and Hirshfeld-inspired integration scheme.[43] The LDA atomic electron densities provided on the ABINIT homepage[52] were employed in the Hirshfeld-inspired integrations. Further computational details are given in the Supporting Information.

3. RESULTS AND DISCUSSION

3.1. Preliminary Considerations from DFT-Chemical Pressure Analysis. As a prelude to our discussion of the structural chemistry in the Mn−Si−C system, let us begin by considering the reactivity of the system's binary phases toward ternary phase formation. Similar to our earlier examination of the Ca−Cu−Cd system, many of the features of the Mn-rich Mn−Si−C ternary phases can be anticipated by DFT-Chemical Pressure (CP) analysis[41−43,53] of their binary neighbors. Along the Mn−C edge, a number of complex carbide phases are encountered, such as Mn_3C (Fe_3C-type)[23] and Mn_7C_3,[54−56] in which the C atoms appear in trigonal prisms with various degrees of face-capping. In the Mn−Si system, the Mn-rich region contains complex tetrahedral close-packed (TCP) phases, which are subject to a high degree of Mn/Si mixed occupancy, including the R-$Mn_{85.5}Si_{14.5}$[57] and ν-$Mn_{81.5}Si_{18.5}$[22] phases.

We set out on our exploration of the local pressures in these phases with simple examples of carbide and TCP arrangements: Mn_3C and a hypothetical Mn_3Si phase in an archetypical TCP structure, the Cr_3Si type (a likely candidate for the low-temperature polymorph of Mn_3Si stable below 677 °C whose structure has yet to be determined).[58] The structures of these phases are shown in Figure 1. Mn_3C (right structure) consists of sheets of edge- and vertex-sharing $C@Mn_6$ trigonal prisms

(yellow), which are stacked so that each prism's rectangular faces are capped with a Mn atom from a neighboring prism (dashed lines). Mn_3Si, on the other hand, adopts a very different structure (left panel): the Si atoms are placed at the points of a body-centered cubic lattice, while the Mn atoms are arranged in the faces of the cell so as to create icosahedral coordination around the Si atoms (purple polyhedron).

In Figure 2a, we compare the DFT-CP schemes calculated for these structures, representing the pressure distribution
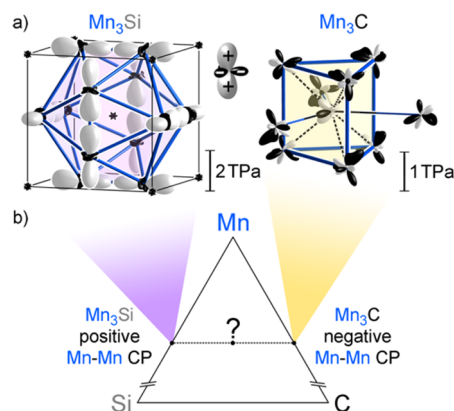

Figure 2. Complementary chemical pressure (CP) schemes of Mn_3C and Cr_3Si-type Mn_3Si, a hypothetical representative of tetrahedral close-packed (TCP) Mn−Si phases. (a) DFT-CP anisotropies plotted for the coordination environments of the C and Si atoms in the two structures (see text for plotting conventions). (b) Updated scheme for frustration in the Mn−Si−C system: distinct geometries of Mn−Si and Mn−C phases favor phase segregation, while their complementary CP schemes provide a driving force for intergrowth.

around each atom with a radial plot. The distance of the radial surface from the atomic center is proportional to the magnitude of the sum of pressures experienced by the atom along that direction. The sign of the pressure is given by the color of the surface: black for negative pressure where contraction is energetically favorable locally, white for positive pressure where expansion is preferred.

The CP scheme for Mn_3Si offers a straightforward picture: the scheme is dominated by white lobes pointing along the Mn−Mn contacts in the faces of the unit cell. The presence of positive pressures at these points in the structure are consistent with the short Mn−Mn distances here; at 2.18 Å (LDA-DFT optimized structure), these represent the shortest contacts in the crystal structure. The desire to expand the structure to relieve these pressures is resisted by the remainder of the contacts in the phase, all of which exhibit relatively small negative CPs. For the Si atoms at the cell corner and centers, the result is 12 narrow CP lobes that point toward their Mn neighbors. The formation of optimal Mn−Si contacts in this phase is thus impeded by the emergence of Mn−Mn repulsion.

Although the scheme of Mn_3C is more complex, overall its major features are the opposite of those observed for Mn_3Si. The C atom at the center of the tricapped trigonal prism exhibits both positive and negative CP lobes, with the positive lobes directed toward the Mn atoms of the prism and the negative lobes pointing to capping atoms. However, the magnitudes of these pressures are not equally balanced: the average over the whole C atom CP surface corresponds to +231 GPa, indicating that the positive CPs are more intense. Overall, then, the C atom is too big for its coordination environment in

this structure. The surrounding Mn−Mn contacts are then largely punctuated with negative CP features, confirming that the C atom's relatively large size leads to the stretching of the Mn sublattice.

Mn_3C and Mn_3Si thus represent opposite scenarios for atomic packing in Mn-rich solid state compounds (Figure 2b). In one, the minority atoms are too small relative to the sites offered by the Mn sublattice, leading to positive CPs along the Mn−Mn contacts. In the other, the minority atoms are too large for their environments, with negative CPs emerging at the Mn−Mn contacts.

The concept of frustrated interactions and the complementarity of these CP schemes together provide a simple way to interpret the crystal structures for Mn−Si−C phases that will form the focus of this Article. The positive CPs between the Mn atoms surrounding the Si atoms and the negative CPs between the Mn atoms around the C atoms can be mutually relieved as the expansion of the former contacts is coupled with the contraction of the latter ones. At the same time, Si and C are distinct enough from each other that they will require quite different geometrical environments, which would tend to promote the spatial segregation of these two elements in the crystal structures. As we will see in the next sections, these competing driving forces bringing Si and C together and pulling them apart leads to a diverse series of carbide/intermetallic intergrowth phases.

3.2. Synthesis and Characterization. Inspired by the prospect of chemical frustration arising in intermetallic carbide systems, and side products encountered by one of our group members while engaged in synthesis in the Mn−Si system, we carried out an experimental exploration of the Mn-rich corner of the Mn−Si−C system. Combinations of the elements in various ratios were pressed into pellets, arc-melted, and then annealed for 5 to 7 days to allow for the maximum possible sample homogeneity and crystal quality. The ingots that resulted were brittle, and easily crushed, with some of the broken fragments being sufficiently crystalline for structure determination with single crystal X-ray diffraction.

Examination of the crystals' diffraction patterns indicated that we obtained two new phases, distinct from the Mn_5SiC[31,32] and Mn_8Si_2C[33,34] compounds described previously for this system (Table 1). Both new cells were monoclinic, with one exhibiting a C-centered cell with dimensions $a = 10.28$ Å, $b = 7.79$, $c = 6.37$, and $\beta = 119°$, while the other showed a primitive cell of $a = 6.41$, $b = 7.66$, $c = 10.49$, and $\beta = 106°$ (some similarities may be apparent in these two sets of cell parameters; somewhat surprisingly, these are for the most part accidental rather than reflecting the many geometrical features shared by the two phases). Inspection of the systematic absences for these two crystal structures pointed to the space groups $C2/m$ and $P2_1/m$, respectively, which were confirmed by the results of the subsequent structure solution and refinement. The refinements revealed clearly distinguishable Mn, Si, and C sites in the structures, with no clear indications of mixed occupancy.[59] The final stoichiometries determined from the diffraction data for the phases are $Mn_{16}SiC_4$ and $Mn_{17}Si_2C_4$, respectively.

Once the formulas for the two structures were known, we carried out more targeted syntheses aimed at their specific compositions. Powder X-ray diffraction data on the resulting samples indicate $Mn_{16}SiC_4$ and $Mn_{17}Si_2C_4$ can be prepared as the major phases in the synthesis products. However, other phases with similar Mn:(Si/C) ratios, particularly Mn_5SiC, could not be entirely eliminated.

To investigate the possible role that magnetic ordering on the Mn atoms plays in these structures, we carried out magnetization measurements on the phases as a function of temperature and applied field. As is described in the Supporting Information, the magnetic properties of $Mn_{16}SiC_4$ and $Mn_{17}Si_2C_4$ show similarities to those of Mn_5SiC,[32] but with moments at least 10 times smaller in magnitude (small fractions of a Bohr magneton per Mn atom). Based on these data, we conclude that magnetic effects are unlikely to significantly influence the structural chemistry in this system. Nonspin-polarized calculations should then suffice for exploring the idea of epitaxial stabilization in these compounds.

3.3. The Crystal Structure of $Mn_{16}SiC_4$. The structures of these two new Mn−Si−C phases can be readily understood in terms of the simultaneous repulsion and attraction between Mn−Si and Mn−C interactions. In $Mn_{16}SiC_4$, the simpler of the two phases, the coordination environments of the C and Si, closely resemble those in Mn_3C and our postulated Cr_3Si-type Mn_3Si phase (Figure 3). The Si atoms center Mn_{12} icosahedra,
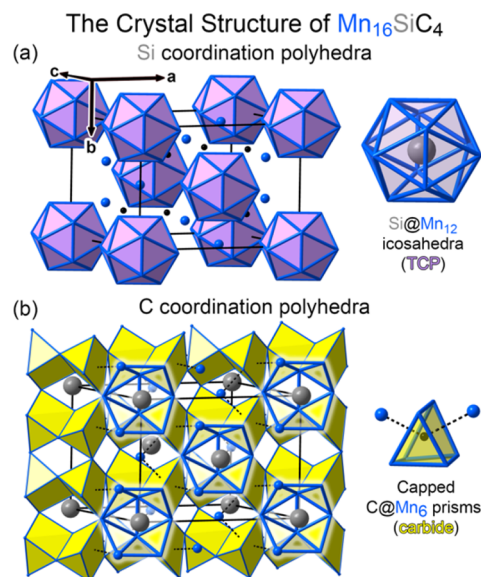

Figure 3. The crystal structure of $Mn_{16}SiC_4$, viewed in terms of its (a) Si-centered icosahedra and (b) capped $C@Mn_6$ trigonal prisms. As will be described in more detail below, these polyhedra are the key components of respectively tetrahedral close-packed (TCP) and carbide domains in the structure.

as they would in the Cr_3Si type, while the C atoms occur in Mn_6 trigonal prisms with additional Mn capping atoms (two capping Mn atoms here, rather than three as in Mn_3C). In addition to these geometrical similarities, the compositions of the Si and C coordination polyhedra also closely resemble the binary phases: the near neighbors to these atoms are exclusively Mn. At the level of individual coordination polyhedra, then, there is a clear segregation of Mn−Si and Mn−C interactions as expected from their geometrical incompatibility.

The favorability of an interface between these interactions, however, is evident in the large number of shared Mn atoms between the Si- and C-centered polyhedra. In Figure 3b, this is illustrated by showing the placement of the Si atoms in the spaces between the $C@Mn_6$ prisms. The shapes of the Si atoms' icosahedral environments are evident in these spaces, reflecting that half of the triangular faces of these prisms are shared with an icosahedron.

This theme of an intimate intergrowth of TCP and carbide regions can be extended to the finer details of the $Mn_{16}SiC_4$ structure and easily generalized to the more complex $Mn_{17}Si_2C_4$ structure. If we look to the surroundings of a $Si@Mn_{12}$ icosahedron in $Mn_{16}SiC_4$, a more extensive TCP region becomes apparent (Figure 4). To see this, we begin with one

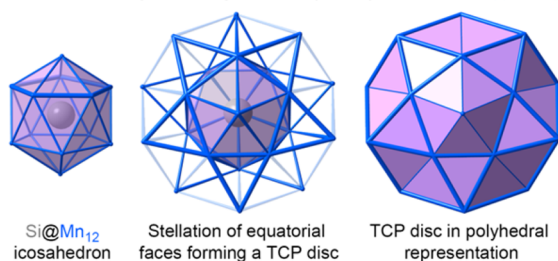**Figure 4.** A TCP motif useful for visualizing the packing of atoms within the $Mn_{16}SiC_4$ structure. All symmetry-distinct Mn and Si sites belong to these discs; only the C atoms remain unaccounted for.

icosahedron and note that each of the 10 triangular faces around its equator is capped by a Mn atom. This stellation leads to a ring of new tetrahedra that, together with the original icosahedron, forms a disc in which all interstitial spaces are tetrahedral. This disc includes instances of all symmetry-distinct Mn sites (Mn1–Mn6) in the $Mn_{16}SiC_4$ structure, making it convenient for visualizing the architecture of the phase.

In Figure 5a, we show the interconnections between the TCP discs in $Mn_{16}SiC_4$. The discs are linked through face-sharing along the c direction, creating strips of TCP packing. Along the b-axis, these strips are connected via shared edges. Together, these linkages along c and b fuse the discs into a rectangular array in the (100) plane. This layer forms the base of the structure's unit cell. As the TCP discs account for all Mn atoms in the crystal structure, several of the atoms on these

discs must also contribute to the carbide portions of the structure. In Figure 5b–c, we illustrate how $C@Mn_6$ trigonal prisms grow from this TCP layer. We start by highlighting in Figure 5b the triangular faces of the TCP discs that are shared with the trigonal prisms. Then, in Figure 5c, we add the trigonal prisms to these highlighted faces.

The newly added trigonal prisms occur in pairs linked through shared edges, which are further connected through shared vertices along b. The conical surfaces of the TCP discs below lead to each of the trigonal prism pairs being inclined relative to the page. The prism orientations undulate as they share faces with the right or left sides of the TCP discs. This buckling of the carbide prisms has an important structural consequence: it creates a grid of pentagonal hollows with the same periodicity as the TCP layer beneath it (thick cylinders in Figure 5c). These hollows provide points for the growth of another TCP layer (related by the crystallographic C-centering to the original layer), as is shown in Figure 5d. The full structure is generated through the repetition of this growth of alternating carbide and TCP layers (Figure 5e, f).

These geometrical features can be related to our earlier considerations about frustration and epitaxial stabilization in the Mn–C–Si system (Figure 2b). $Mn_{16}SiC_4$ lies in the phase diagram almost directly along the line connecting Mn_3Si and Mn_3C, where the tension between the immiscibility of TCP and carbide regions and the potential for complementary CPs between Mn–Si and Mn–C interactions is highest. The overall crystal structure exhibits the clear formation of Mn–Si based TCP domains and Mn–C carbide domains with no Si–C close contacts, as expected from their geometrical incompatibility. At the same time, the sharing of Mn atoms between the TCP and carbide portions is extensive. In fact, with the exception of Mn6 (whose interactions are mostly with other Mn atoms), all of the Mn sites in the structure exhibit close contacts to both Si and C atoms. This trend affirms the mutual stabilization between Mn–Si and Mn–C interactions suggested by our CP analysis of the original binary structures.
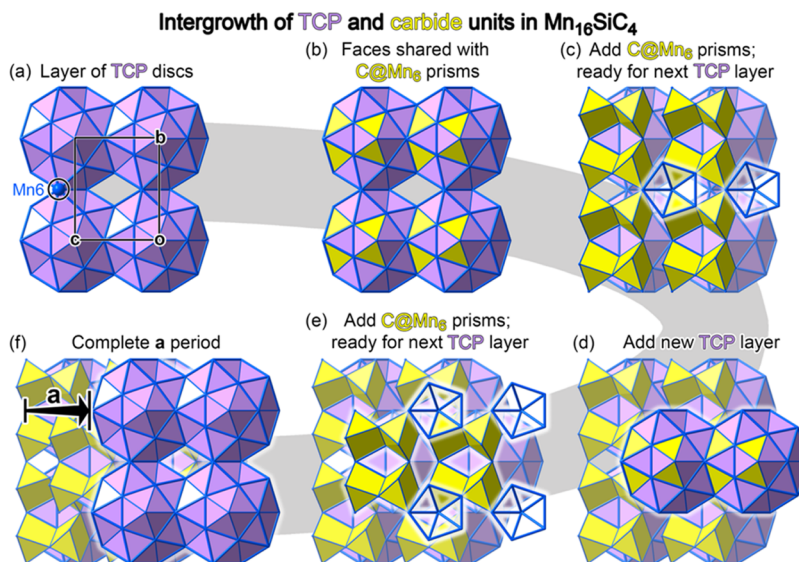

Figure 5. The crystal structure of $Mn_{16}SiC_4$ viewed as an intergrowth of tetrahedral close-packed (TCP) and carbide domains. (a) A layer of TCP discs at the base of the unit cell in the bc plane. (b) Color coding of the faces of the TCP discs in (a), with yellow indicating faces that are shared with $C@Mn_6$ trigonal prisms. (c) The addition of some of these $C@Mn_6$ prisms, highlighting the pentagonal hollows into which (d) the lower pentagonal tips of the next layer of TCP discs nestle (with fusion through shared triangular faces occurring). (e–f) The repetition of the deposition of carbide and TCP layers to complete the repeat period of the structure along a. See text for a discussion of the Mn6 site.

3.4. The Crystal Structure of $Mn_{17}Si_2C_4$. Similar structural features and trends can be discerned in the crystal structure of the second new phase described in this Article, $Mn_{17}Si_2C_4$ (Figure 6). To see the similarities to the $Mn_{16}SiC_4$

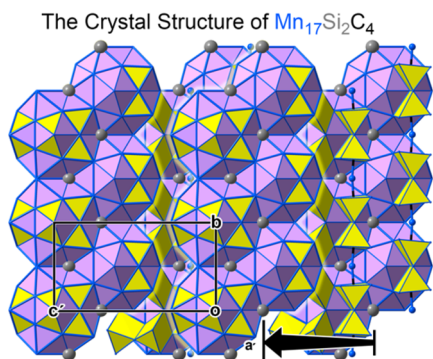**Figure 6.** The crystal structure of $Mn_{17}Si_2C_4$ following the conventions of Figure 5. A more detailed illustration of the architecture of this phase can be found in the Supporting Information as Figure S1.

phase, it is convenient to transform the unit cell from that used in the original indexation of the crystal's diffraction pattern to $\mathbf{a}' = \mathbf{a} + \mathbf{c}$, $\mathbf{b}' = \mathbf{b}$, and $\mathbf{c}' = -\mathbf{c} - 2\mathbf{a}$ (which is unconventional due to the β angle being further from 90° than the original: $\beta' = 25°$ or $180° - 25° = 155°$ vs $\beta = 106°$). In this setting, an array of TCP discs is again present in sheets running parallel to the (100) basal plane of the unit cell (Figure 6), which alternate with layers of capped $C@Mn_6$ trigonal prisms (yellow). This time, however, the Si atoms appear both in the icosahedral centers and at some shared vertices where three TCP discs meet (the Si1 site, gray spheres in Figure 6).

Another difference from the $Mn_{16}SiC_4$ structure is in how these TCP discs are arranged. Rather than lying along a rectangular grid as in Figure 5a, the discs now occur in strips of discs (joined in a zigzag fashion through shared faces) that run along the b direction. Some further tetrahedra can be found linking these strips to each other, creating a slightly more extensive network of tetrahedra. However, none of them link the two arrays of TCP discs through a network of face-sharing triangles; the TCP connectivity is then broken between strips.

Overall, the features of this crystal structure also follow the expectations of simultaneous attraction and repulsion between Mn−Si and Mn−C interactions described in section 3.1. Every Mn site in the structure partakes in the coordination of the C atoms as either a vertex of the trigonal prisms or as a capping atom (although some of Mn−C distances for the capping Mn atoms can be quite large, up to 3.02 Å). At the same time, all of the Mn atoms except those at the Mn6 and Mn7 sites (at the edges of the TCP strips) are simultaneously participating in bonding with the Si atoms. And yet, despite these extensive interactions of Mn atoms with both Si and C atoms, the Si−C distances in the structure never fall below 3.4 Å. This observation and the preservation of the C and Si coordination environments from the binary Mn−Si and Mn−C phases, respectively, affirms the immiscibility of Mn−Si and Mn−C interactions.

3.5. Chemical Pressure Relief in Mn_3Si−Mn_3C Intergrowths. In our above discussion of the structures of $Mn_{16}SiC_4$ and $Mn_{17}Si_2C_4$, we saw that their features could be rationalized in terms of epitaxial stabilization at the interface between Mn−Si TCP and Mn−C carbide domains. In this

hypothesis, the driving force for the intergrowth of Mn−Si and Mn−C domains arises from the complementary CP schemes of the binary silicide and carbide phases. Let us now examine whether signs of epitaxial stabilization can also be perceived in their electronic structures.

The complementarity of CP schemes for the Mn−C and Mn−Si binary compounds is illustrated again in Figure 7a−b. Here, the dominant pressures within the Mn sublattices are seen to be positive in the TCP representative Mn_3Si and negative in the carbide Mn_3C. A look at the sizes of the CP lobes and scale bars in these images reveals that the magnitudes of these pressures are not equal. The positive Mn−Mn pressures in the Mn−Si TCP phase are significantly more intense than their negative counterparts in Mn_3C. A high priority in the structural preferences of a Mn−Si−C phase should then be the release of the Mn−Mn steric congestion around the Si atoms.

In Figure 7c−e, we present the CP schemes for the TCP regions of the Mn_5SiC, $Mn_{16}SiC_4$, and $Mn_{17}Si_2C_4$ phases, moving from the most Si-rich to the most C-rich of these ternary compounds. The Si are represented as spheres so that we can focus on the progression of CPs on the Mn atoms (the net CPs on the Si and C change little from the binaries and are generally smaller in the ternaries). In all these ternaries, the maximum positive CP lobes between the Mn atoms have become substantially lower relative to those calculated for Mn_3Si. Smaller changes occur for the negative Mn−Mn CPs, confirming that relieving overly short Mn−Mn contacts has been given priority.

Trends can also be perceived across the CP schemes of the ternary phases. For the phase with the smallest C content, Mn_5SiC, zigzag chains of Mn−Mn positive CPs are seen running vertically up and down the plot in Figure 7c. These chains are rather evenly distributed through the structure and strongly associated with the Si-centered polyhedra. Upon moving to $Mn_{17}Si_2C_4$ with a slightly higher fraction of C in the phase, the positive Mn−Mn CPs remain directed along chains (this time meandering through the structure rather than following simple zigzag arrangements; see Figure 7d). However, more space is now present between these strands of positive pressure. Regions dominated by negative CPs now appear, providing greater separation between the chains of positive CPs.

In $Mn_{16}SiC_4$ with the largest concentration of C (Figure 7e), the positive CPs are further reduced, with the lobes generally being much smaller than those plotted for the other phases. In addition, the positive CPs are no longer localized to the Mn−Mn contacts in the Si coordination polyhedra. The largest positive Mn−Mn CPs here are focused in the openings in the TCP regions where four TCP discs meet.

This progression points toward the gradual reduction in the Mn−Mn congestion around the Si atoms as C atoms are added to the structure. One interpretation of this result is that the less dense packing of the Mn atoms in the C-centered polyhedra provides space to allow the expansion of the Mn−Mn contacts around the Si atoms. Some support for this mechanism of CP relief is found in the geometries of these polyhedra. The $Si@Mn_{12}$ icosahedra of the Mn−Si−C phases are much more ideal than is achievable within the constraints of the Cr_3Si type, suggesting relaxation has occurred on moving to the ternaries. The $C@Mn_6$ prisms, meanwhile, are quite distorted in the Mn−Si−C phases relative to those found in Mn_3C. Regardless of the specific geometrical mechanism, however, the CPs in the
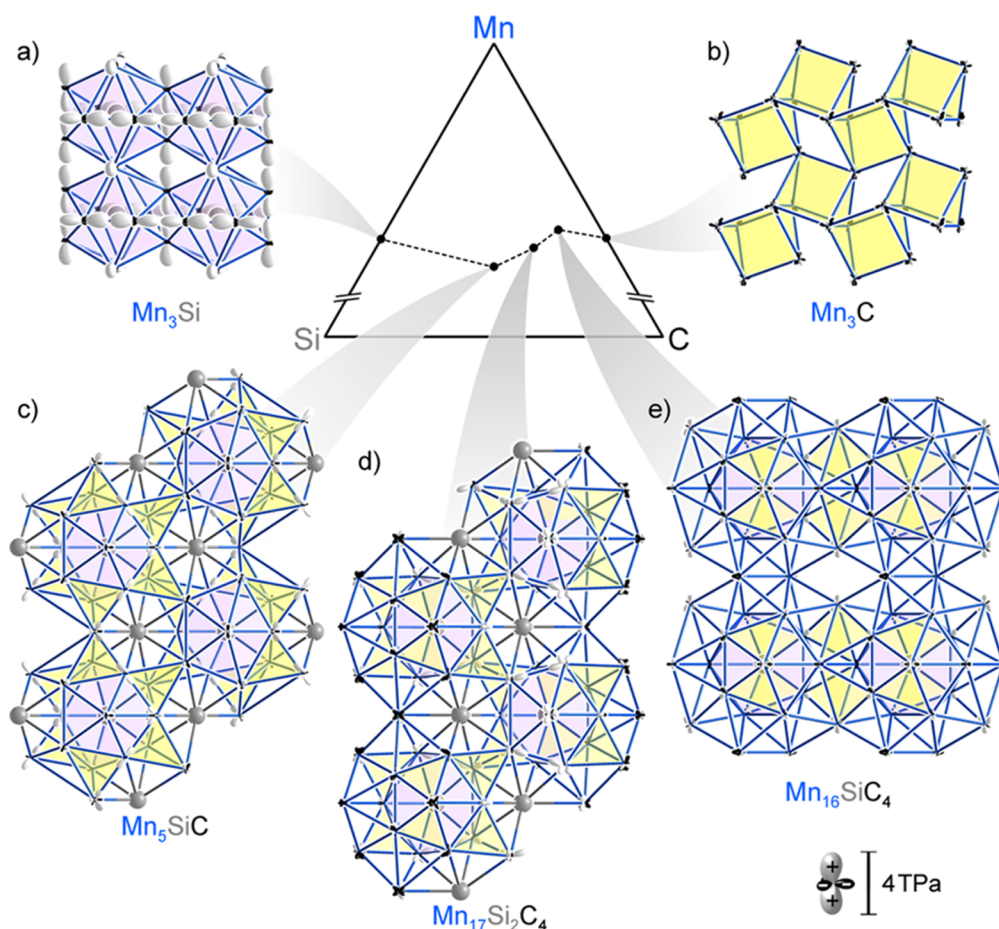
Figure 7. Comparison of the Mn−Mn chemical pressures (CPs) across a series of TCP-carbide intergrowths in the Mn−Si−C system. (a and b) CPs in the TCP and carbide end members of the series, represented by a Cr$_3$Si-type Mn$_3$Si phase and Mn$_3$C, respectively. The dominant Mn−Mn pressures in these structures are of opposite sizes due to the Si being small for its environment in Mn$_3$Si and C being large for its site in Mn$_3$C. (c−e) The corresponding plots of the TCP regions of Mn$_5$SiC, Mn$_{17}$Si$_2$C$_4$, and Mn$_{16}$SiC$_4$. The largest effect of the intergrowth appears to be the substantial reduction of the positive Mn−Mn CPs in the TCP regions. Si atoms are represented by gray spheres. Carbon atoms are not shown to avoid confusion with the black used in the plotting of the CP lobes, but faces of their Mn$_6$ trigonal prisms are indicated in yellow. See text for CP plotting conventions.

ternary phases are less severe than in the sum of the binary phases. This CP relief supports the hypothesis that epitaxial stabilization serves as the driving force allowing the intergrowth of TCP and carbide features in these compounds.

How does the strength of this epitaxial stabilization effect compare energetically to the packing frustration involved in combining the Mn−Si and Mn−C domains into a single structure? Some sense of this can be obtained by calculating reaction energies for the formation of the intergrowth phases from their simpler components, such as 4Mn$_3$C(s) + Mn$_3$Si(s) + Mn(s) → Mn$_{16}$SiC$_4$(s). From our DFT calculations, such reactions appear to be energy neutral (at 0 K, in the absence of magnetic ordering) to within 1 kcal/mol per atom (see the Supporting Information for further details). Given the variety of Mn−Si and Mn−C binary phases that could form alternative products, we suspect that the formation of the intergrowth phases is slightly disfavored at low temperatures, indicating that packing frustration wins out in the absence of entropic effects. The effect of epitaxial stabilization is evident in the accessibility of the intergrowth structures at elevated temperatures and the geometrical details of these intergrowths.

4. CONCLUSIONS

In this Article, we have explored how frustration can be induced in intermetallic carbides, using the Mn−Si−C system as a model. Analysis of binary phases in this system and their chemical pressure schemes highlighted the potential for competing interactions. In particular, at the Mn-rich corner, the preference for carbide geometries along the Mn−C edge of the system would struggle to reconcile itself with the prevalence of tetrahedral close-packed (TCP) geometries at the Mn−Si edge. However, chemical pressure (CP) analysis on representatives for the binary systems, Mn$_3$C and a Cr$_3$Si-type Mn$_3$Si phase, hints that there are advantages to mixing carbide and TCP features. The Mn−Mn interactions in the binary structures show opposite signs in their CPs, which could be relieved by placing Mn atoms at the interface between Si- and C-containing domains.

With this analysis, the stage was set for interpreting a series of complex ternary phases in this system. The new compounds Mn$_{16}$SiC$_4$ and Mn$_{17}$Si$_2$C$_4$, along with the previously described Mn$_5$SiC and Mn$_8$Si$_2$C, appear to trace out a line connecting Mn$_3$C and Mn$_3$Si at the Mn-rich corner of the diagram (Figure 2b). These four complex ternary phases thus represent intermediate points between full carbide and TCP end-

members of this series, and the structural features of these compounds can be rationalized from this placement. Their structures are built from domains of capped $C@Mn_6$ trigonal prisms intergrown with TCP regions. These two domain types are reminiscent of the Mn-rich binary phases in the Mn–C and Mn–Si systems, respectively, indicating that a form of microscopic phase segregation has taken place. At the same time, the interface between these domains appears to be stabilizing, as the majority of the Mn atoms are positioned to participate in both Mn–Si and Mn–C interactions.

In this way, the complex structures in the Mn–Si–C system can be interpreted as different compromises between attractive and repulsive forces between Mn–C and Mn–Si interactions. This conclusion is similar to that we reached for the formation of the Bergman-type quasicrystal approximant $Ca_{10}Cd_{27}Cu_2$ in the Ca–Cu–Cd system, in which geometrical frustration between Ca–Cd and Cu–Cd interactions appears to be driven by the possibility of CP release at their interfaces. Both the Mn–Si–C and Ca–Cd–Cu systems seem to run counter to the usual expectation that such interfaces would be occasions for epitaxial strain. Instead, a form of epitaxial stabilization seems to occur, where the opportunities for the cancellation of opposite CPs arise. We are looking forward to seeing whether this epitaxial stabilization mechanism may serve as a general principle for the design of frustrated systems.

ASSOCIATED CONTENT

Supporting Information

The Supporting Information is available free of charge on the ACS Publications website at DOI: 10.1021/jacs.5b10355.

> Crystallographic data for $Mn_{16}SiC_4$ and $Mn_{17}Si_2C_4$, including atomic coordinates, atomic displacement parameters, and selected interatomic distances; an expanded version of Figure 6; powder X-ray diffraction data for samples containing $Mn_{16}SiC_4$ or $Mn_{17}Si_2C_4$ as majority phases; magnetic properties data; consideration of a possible role of oxygen impurities in the title phases; further computational details; DFT-CP analysis of the experimentally observed high-temperature Mn_3Si phase (BiF_3-type); LDA-DFT optimized coordinates and total energies for all structures analyzed with the DFT-CP method (PDF)
> Crystallographic data for $Mn_{16}SiC_4$ (CIF)
> Crystallographic data for $Mn_{17}Si_2C_4$ (CIF)

AUTHOR INFORMATION

Corresponding Author
*danny@chem.wisc.edu

Notes
The authors declare no competing financial interest.

ACKNOWLEDGMENTS

REFERENCES

(1) Hamley, I. W. *Introduction to Soft Matter: Synthetic and Biological Self-Assembling Materials*, revised edition; John Wiley & Sons: Chichester, U.K.; Hoboken, NJ, 2007.

(2) Nelson, D. R. *Phys. Rev. B: Condens. Matter Mater. Phys.* **1983**, 28, 5515–5535.

(3) Miracle, D. B. *Nat. Mater.* **2004**, 3, 697–702.

(4) Egami, T.; Levashov, V.; Aga, R.; Morris, J. R. *Metall. Mater. Trans. A* **2008**, 39, 1786–1790.

(5) Hirata, A.; Kang, L. J.; Fujita, T.; Klumov, B.; Matsue, K.; Kotani, M.; Yavari, A. R.; Chen, M. W. *Science* **2013**, 341, 376–379.

(6) Mosseri, R.; Sadoc, J.-F. *C. R. Phys.* **2014**, 15, 90–99.

(7) Inoue, A. *Acta Mater.* **2000**, 48, 279–306.

(8) Ganesh, P.; Widom, M. *Phys. Rev. B: Condens. Matter Mater. Phys.* **2008**, 77, 014205.

(9) Wu, Z. W.; Li, M. Z.; Wang, W. H.; Liu, K. X. *Nat. Commun.* **2015**, 6, 6035.

(10) Fredrickson, D. C.; Lee, S.; Hoffmann, R. *Angew. Chem., Int. Ed.* **2007**, 46, 1958–1976.

(11) Conrad, M.; Harbrecht, B.; Weber, T.; Jung, D. Y.; Steurer, W. *Acta Crystallogr., Sect. B: Struct. Sci.* **2009**, 65, 318–325.

(12) Weber, T.; Dshemuchadse, J.; Kobas, M.; Conrad, M.; Harbrecht, B.; Steurer, W. *Acta Crystallogr., Sect. B: Struct. Sci.* **2009**, 65, 308–317.

(13) Greedan, J. E. *J. Mater. Chem.* **2001**, 11, 37–53.

(14) Gignoux, D.; Schmitt, D. *J. Alloys Compd.* **2001**, 326, 143–150.

(15) Lacroix, C. *J. Phys. Soc. Jpn.* **2010**, 79, 011008.

(16) Cava, R.; Holman, K.; McQueen, T.; Welsh, E.; West, D. V.; Williams, A. In *Introduction to Frustrated Magnetism*; Lacroix, C., Mendels, P., Mila, F., Eds.; Springer: Berlin Heidelberg, 2011; Vol. 164, pp 131–154.

(17) Zvyagin, A. A. *Low Temp. Phys.* **2013**, 39, 901–922.

(18) Hadler, A. B.; Harris, N. A.; Fredrickson, D. C. *J. Am. Chem. Soc.* **2013**, 135, 17369–17378.

(19) Jain, S. C.; Harker, A. H.; Cowley, R. A. *Philos. Mag. A* **1997**, 75, 1461–1515.

(20) Pearson, W. B. *The Crystal Chemistry and Physics of Metals and Alloys*; Wiley-Interscience: New York, 1972.

(21) Bradley, A. J.; Thewlis, J. *Proc. R. Soc. London, Ser. A* **1927**, 115, 456–471.

(22) Shoemaker, C. B.; Shoemaker, D. P. *Acta Crystallogr., Sect. B: Struct. Crystallogr. Cryst. Chem.* **1971**, 27, 227–235.

(23) Dierkes, H.; Dronskowski, R. *Z. Anorg. Allg. Chem.* **2014**, 640, 3148–3152.

(24) L'Heritier, P.; Chaudouet, P.; Fruchart, R.; Shoemaker, C. B.; Shoemaker, D. P. *J. Solid State Chem.* **1985**, 59, 54–59.

(25) Bodak, O. I.; Marusin, E. P.; Fundamenskii, V. S.; Bruskov, V. A. *Kristallografiya* **1982**, 27, 1098–1101.

(26) Marusin, E. P.; Bodak, O. I.; Tsokol, A. O.; Fundamenskii, V. S. *Kristallografiya* **1985**, 30, 581–583.

(27) Tsokol, A. O.; Bodak, O. I.; Marusin, E. P. *Kristallografiya* **1986**, 31, 73–75.

(28) Khalili, M. M.; Bodak, O. I.; Marusin, E. P.; Pecharskaya, A. O. *Kristallografiya* **1990**, 35, 337–341.

(29) Khalili, M. M.; Bodak, O. I.; Marusin, E. P.; Pecharskaya, A. O. *Kristallografiya* **1990**, 35, 1378–1380.

(30) Moss, M. A.; Jeitschko, W. *J. Alloys Compd.* **1992**, 182, 157–164.

(31) Spinat, P.; Fruchart, R.; Kabbani, M.; Herpin, P. *Bull. Soc. Fr. Mineral. Cristallogr.* **1970**, 93, 171–184.

(32) Spinat, P.; Herpin, P. *Bull. Soc. Fr. Mineral. Cristallogr.* **1976**, 99, 13–20.

(33) Spinat, P.; Senateur, J. P.; Fruchart, R.; Herpin, P. *C. R. Acad. Sci., Ser. C* **1972**, 274, 1159–1162.

(34) Spinat, P.; Brouty, C.; Whuler, A.; Herpin, P. *Acta Crystallogr., Sect. B: Struct. Crystallogr. Cryst. Chem.* **1975**, 31, 541–547.

(35) Gokhale, A. B.; Abbaschian, G. J. *Binary Alloy Phase Diagrams* **1990**, *3*, 2602−2604.

(36) Oszlányi, G.; Sütő, A. *Acta Crystallogr., Sect. A: Found. Crystallogr.* **2004**, *60*, 134−141.

(37) Oszlányi, G.; Sütő, A. *Acta Crystallogr., Sect. A: Found. Crystallogr.* **2005**, *61*, 147−152.

(38) Palatinus, L.; Chapuis, G. *J. Appl. Crystallogr.* **2007**, *40*, 786−790.

(39) Petříček, V.; Dušek, M.; Palatinus, L. *Z. Kristallogr. - Cryst. Mater.* **2014**, *229*, 345−352.

(40) *Probe for EPMA User's Guide and Reference*; Donovan, J. J., Kremswer, D., Fournelle, J., Karsten, G., Eds.; Probe Software, Inc.: Eugene, OR, 2013.

(41) Fredrickson, D. C. *J. Am. Chem. Soc.* **2012**, *134*, 5991−5999.

(42) Engelkemier, J.; Berns, V. M.; Fredrickson, D. C. *J. Chem. Theory Comput.* **2013**, *9*, 3170−3180.

(43) Berns, V. M.; Engelkemier, J.; Guo, Y.; Kilduff, B. J.; Fredrickson, D. C. *J. Chem. Theory Comput.* **2014**, *10*, 3380−3392.

(44) Kresse, G.; Furthmüller, J. *Phys. Rev. B: Condens. Matter Mater. Phys.* **1996**, *54*, 11169−11186.

(45) Kresse, G.; Furthmüller, J. *Comput. Mater. Sci.* **1996**, *6*, 15−50.

(46) Vanderbilt, D. *Phys. Rev. B: Condens. Matter Mater. Phys.* **1990**, *41*, 7892−7895.

(47) Gonze, X.; Rignanese, G.-m.; Verstraete, M.; Beuken, J.-m.; Pouillon, Y.; Caracas, R.; Raty, J.-y.; Olevano, V.; Bruneval, F.; Reining, L.; Godby, R.; Onida, G.; Hamann, D. R.; Allan, D. C. *Z. Kristallogr.* **2005**, *220*, 558−562.

(48) Gonze, X.; Amadon, B.; Anglade, P.-M.; Beuken, J.-M.; Bottin, F.; Boulanger, P.; Bruneval, F.; Caliste, D.; Caracas, R.; Côté, M.; Deutsch, T.; Genovese, L.; Ghosez, P.; Giantomassi, M.; Goedecker, S.; Hamann, D. R.; Hermet, P.; Jollet, F.; Jomard, G.; Leroux, S.; Mancini, M.; Mazevet, S.; Oliveira, M. J. T.; Onida, G.; Pouillon, Y.; Rangel, T.; Rignanese, G.-M.; Sangalli, D.; Shaltaf, R.; Torrent, M.; Verstraete, M. J.; Zerah, G.; Zwanziger, J. W. *Comput. Phys. Commun.* **2009**, *180*, 2582−2615.

(49) Goedecker, S.; Teter, M.; Hutter, J. *Phys. Rev. B: Condens. Matter Mater. Phys.* **1996**, *54*, 1703−1710.

(50) Hartwigsen, C.; Goedecker, S.; Hutter, J. *Phys. Rev. B: Condens. Matter Mater. Phys.* **1998**, *58*, 3641−3662.

(51) The Fredrickson Group DFT Chemical Pressure Package is freely available at URL http://www.chem.wisc.edu/~danny/software/dftcpp/.

(52) Gonze, X. LDA density files for the Hirschfeld atomic charge analysis. http://www.abinit.org/downloads/all_core_electron (Last accessed: Sept. 22, 2015).

(53) Berns, V. M.; Fredrickson, D. C. *Inorg. Chem.* **2014**, *53*, 10762−10771.

(54) Bouchaud, J. P. *Ann. Chim. (Paris)* **1967**, *2*, 353−366.

(55) Hájek, B.; Karen, P.; Brožek, V. *Collect. Czech. Chem. Commun.* **1983**, *48*, 2740−2750.

(56) Karen, P.; Fjellvåg, H.; Kjekshus, A.; Andresen, A. F. *Acta Chem. Scand.* **1991**, *45*, 549−557.

(57) Shoemaker, C. B.; Shoemaker, D. P. *Acta Crystallogr., Sect. B: Struct. Crystallogr. Cryst. Chem.* **1978**, *34*, 701−705.

(58) LDA-DFT calculations indicate that for Mn_3Si the Cr_3Si type has a total energy that is 0.004 eV/formula unit more stable than the BiF_3-type structure observed at high temperature. This energy difference is within the uncertainty expected for the calculation, indicating that the two phases would be close competitors at low temperatures (where entropic factors would be minimized).

(59) It is difficult to completely rule out the possibility that impurity oxygen atoms may partially substitute for carbon in the structure. However, as is detailed in the Supporting Information, the modes of reactivity of oxygen and carbon with manganese are sufficiently different that this scenario is unlikely.